A Novel Conservative Lagrangian Immersed Boundary Method For Wind Turbine Simulations

Iason Tsetoglou, Pierre Bénard, Ghislain Lartigue, Vincent Moureau, Julien Reveillon

A Novel Conservative Lagrangian Immersed Boundary Method for Wind Turbine Simulations

I. Tsetoglou[1], *P. Benard*[1], *G. Lartigue*[1], *V. Moureau*[1] *and J. Reveillon*[1]

[1] *CNRS UMR 6614 - CORIA, France*

iason.tsetoglou@coria.fr

Abstract

This work presents a novel conservative Lagrangian immersed boundary method (CLIB) to solve incompressible viscous fluid flow problems around solid geometries. Classical immersed boundary methods (IBM) are known to face mass and momentum conservation issues at the frontier between solid and fluid. This original method couples the penalty IBM with a Lagrangian volume of solid (VOS) formulation introducing some extra source terms in the governing equations. These terms serve to represent the existence of a solid body inside the fluid domain and give rise to a fully conservative system of equations. Solid mass conservation is guaranteed thanks to a Lagrangian representation of the solid volume fraction field and is proven effectively independent of the grid resolution. The accuracy of the present method is demonstrated by the good agreement of aerodynamic quantities for two-dimensional flows around stationary and mobile (rotating, oscillating) rigid solid bodies with the values found in literature.

1 Introduction

Renewable energy production units, such as wind turbines, involve geometrically complex bodies (rigid or flexible) in motion and in contact with fluids. The study of wind turbine wakes involves high Reynolds number flows around mobile complex geometries and a wide range of temporal and spatial scales. This makes body-fitted computations unaffordable. State-of-the-art computations in wind energy are based on Large-Eddy simulations (LES) coupled with actuator line methods (ALM) where no re-meshing is required (Porté-Agel et al. (2019)). This framework requires the characteristics of the airfoil and its aerodynamic coefficients to model its influence onto the fluid via a momentum source term. An attractive alternative for simulating fluid-structure interaction (FSI) problems involving complex geometries and arbitrarily large movements is the use of immersed boundary methods (IBM). These methods do not need body-fitted meshes due to the ability to allocate grid points within the solid region. The main challenge is the proper modelling of the presence of the immersed solid into the fluid via forcing terms in the governing equations.

The original method was developed by Peskin (1972) to simulate cardiac mechanics and associated blood flow. Since then, the IB methods have been extended to various applications in scientific and engineering fields. Numerous modifications and refinements have been proposed and a number of variants of this approach now exist focusing on the definition of the forcing term (extensive review can be found in Sotiropoulos and Yang (2014)). The forcing term can be represented in a discrete or a continuous manner. The general advantage of continuous forcing is that the formulation is almost independent of the discretization scheme, which makes its integration easier. Hence, the present work focuses on the continuous IBM of penalization with a sharp representation of the solid-fluid interface. Furthermore, the coupling of this method with a Lagrangian volume of solid (VOS) approach results in a fully conservative set of governing equations by introducing extra source terms in the aforementioned equations. This method will be referenced as conservative Lagrangian immersed boundaries (CLIB).

This paper is organized in the following manner. In Section 2 the governing equations and the main numerical tools of this study are presented. The methodology is applied on three validation cases in Section 3: flow past a stationary, a rotating and an oscillating cylinder. Lastly, in Section 4 concluding remarks about the method will be given.

2 Numerical framework

Governing equations

To start, the coupling of the volume of fluid (proposed by Hirt and Nichols (1981)) and the penalty IBM yields the following continuity and momentum equations for the fluid:

$$\frac{\partial}{\partial t}\left(\phi_f\right) + \nabla \cdot \left(\phi_f \boldsymbol{u}_f\right) = 0\,, \tag{1}$$

$$\frac{\partial}{\partial t}\left(\phi_f \boldsymbol{u}_f\right) + \nabla \cdot \left(\phi_f \boldsymbol{u}_f \boldsymbol{u}_f\right) = -\frac{1}{\rho}\nabla P + \frac{1}{\rho}\nabla \cdot \left(\phi_f \boldsymbol{\tau}\right) + \boldsymbol{F}^{s\to f}\,. \tag{2}$$

where $\boldsymbol{u}_f$ is the fluid velocity, ϕ_f the fluid fraction, P is the pressure, $\boldsymbol{\tau} = \mu\left(\nabla \boldsymbol{u}_f + \nabla \boldsymbol{u}_f^T\right)$ the viscous

stress tensor, $\boldsymbol{F}^{s\to f}$ the solid-fluid interaction and ρ the fluid density.

A unified mean velocity field $\boldsymbol{u}$ is introduced, given by:

$$\boldsymbol{u} = \phi_f \boldsymbol{u}_f + \phi_s \boldsymbol{u}_s \,, \tag{3}$$

where $\boldsymbol{u}_s$ is the solid velocity and $\phi_s = (1 - \phi_f)$ the solid fraction. A similar expression is used by Liu et al. (2021) but as a correction to the predicted intermediate velocity to compute the forcing term in a direct forcing IB approach.

In the method presented here, this unified velocity is inserted directly to both the mass and momentum conservation equations (1,2) giving rise to a unique system of equations capable of describing both the fluid and the solid phases. Finally, the governing equations for incompressible flows using the CLIB method read:

$$\nabla \cdot \boldsymbol{u} = \frac{\partial}{\partial t}\left(\phi_s\right) + \nabla \cdot \left(\phi_s \boldsymbol{u}_s\right) , \tag{4}$$

$$\begin{aligned}\frac{\partial \boldsymbol{u}}{\partial t} + \nabla \cdot (\boldsymbol{u}\boldsymbol{u}) = &-\frac{1}{\rho}\nabla P + \frac{1}{\rho}\nabla \cdot \left(\phi_f \boldsymbol{\tau}\right) + \boldsymbol{F^{s\to f}} \\ &+ \frac{\partial}{\partial t}\left(\phi_s \boldsymbol{u}_s\right) + \nabla \cdot \left(\phi_s \boldsymbol{u}_s \boldsymbol{u}_s\right) .\end{aligned} \tag{5}$$

This final set of equations is very similar to the pure fluid equations except for the additional transport terms on the right-hand side (RHS). The volume source term in the RHS of the continuity equation is associated with the solid movement and/or its deformation/dilatation and will be noted as $\mathscr{Q}_s$. The source term in the RHS of the momentum conservation equation is related to volume force applied by the solid on the fluid and will be noted as $\mathscr{P}_s$. This system of equations is fully conservative.

The volume forcing term $\boldsymbol{F}^{s\to f}$ is represented sharply via a penalty term as described in Angot et al. (1999) which constrains the velocity $\boldsymbol{u}$ to be equal to the solid velocity inside the solid region. This is achieved through the use of a masking term χ_s, activated only for $\phi_s > 0$, and a penalization time parameter η, representing the time needed for the mean velocity to reach the target solid velocity. A conventional technique is to set the mask equal to 0 or 1 for fluid and solid nodes respectively, but we wanted to guarantee a continuous application of the force while amplifying the effect at the nodes with small solid fraction values. The penalty term is expressed as follows:

$$\boldsymbol{F}^{s\to f} = \frac{\chi_s}{\eta}\left(\boldsymbol{u}_s - \boldsymbol{u}\right) , \tag{6}$$

$$\chi_s \equiv \sqrt{\phi_s}, \quad \eta \equiv \Delta t \,. \tag{7}$$

Lagrangian solid fraction field

A strong point of this method lies in the use of a Lagrangian framework. Using Lagrangian particles in IBM for the force calculation has already been examined, as in Uhlmann (2005). Here, they are used to define a Lagrangian field of the solid fraction ensuring solid mass conservation.

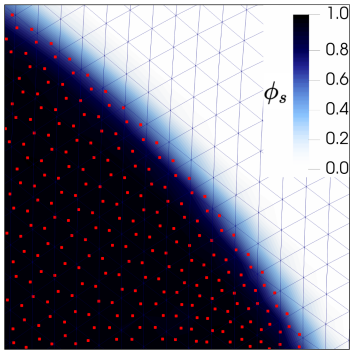

Figure 1: Solid volume fraction field projected onto the Eulerian mesh from the Lagrangian particles (in red).

The procedure of the solid fraction computation consists of two stages. First comes a pre-processing stage where an unstructured mesh representing the solid is generated. Inside each cell of this mesh, we place Lagrangian particles containing information on the solid volume. During the computation stage, before the advection of the velocity at each iteration, the particles are relocated on the Eulerian mesh (depending on the motion of the solid) and then the volume carried by the particles is projected onto the Eulerian mesh resulting in the computation of the local quantity of solid volume, and by extension, the local solid fraction ϕ_s, as illustrated by Fig. 1.

The solid volume $V_{s,i}$ at grid node i is given by:

$$V_{s,i} = \sum_{p|\mathbf{x}_p \in E_i} V_p W_{i,p} \,. \tag{8}$$

The subscript p denotes the properties of the p^{th} particle, E_i is the set of elements adjacent to the grid node i, and $W_{i,p}$ is the weight of the linear interpolation. Its expression reads:

$$W_{i,p} = \frac{|\boldsymbol{x}_p - \boldsymbol{x}_{fi}| \cdot \boldsymbol{S}_{fi}}{\sum_{i' \in \mathcal{N}(E_p)} |\boldsymbol{x}_p - \boldsymbol{x}_{fi'}| \cdot \boldsymbol{S}_{fi'}} \,, \tag{9}$$

where E_p is the element containing particle p, and $\mathcal{N}(E)$ is the set of nodes i' of the element E and $\boldsymbol{S}_{fi'}$ the vector area of the face fi' opposite to the node i. The solid fraction may then be written as:

$$\phi_{s,i} = \frac{V_{s,i}}{V_i} \,. \tag{10}$$

This solid volume fraction is not necessarily equal to one inside the solid because of local errors. ϕ_s is therefore slightly filtered with a conservative diffusive filter where diffusion is non-zero only in the solid, i.e. diffusivity is a constant multiplied by ϕ_s.

Numerical schemes and CLIB implementation

Equations (4) and (5) are solved using the YALES2 flow solver. YALES2 is a massively-parallel finite-volume solver, presented in Moureau et al. (2011). It

is specifically tailored for Large-Eddy Simulation, and relies on a central 4th-order numerical scheme for spatial discretization, and a 4th-order Runge-Kutta like method for the time integration on unstructured grid. The CLIB method is implemented via the following steps at each fluid iteration:

1. **Advancement of solid volume fraction field**

   The Lagrangian solid particles are advanced from time-step $n+1/2$ to $n+3/2$ according to the motion prescribed to the solid and the solid volume fraction $\phi_s^{n+3/2}$ is computed as described in the previous paragraph. Then, at time-step $n+1$:

$$\phi_s^{n+1} = \frac{1}{2}\left[\phi_s^{n+1/2} + \phi_s^{n+3/2}\right] . \tag{11}$$

2. **Computation of CLIB source terms**

   To allow rapid convergence of the predicted velocity to the target $\boldsymbol{u}_s$ at the solid, the CLIB source terms are expressed implicitly as:

$$\mathscr{Q}_s^{n+1} = \left[\frac{\phi_s^{n+3/2} - \phi_s^{n+1/2}}{\Delta t}\right] + \nabla\cdot\left(\phi_s^{n+1}\boldsymbol{u}_s^{n+1}\right) , \tag{12}$$

$$\mathscr{P}_s^{n+1} = \left[\frac{\phi_s^{n+3/2}\boldsymbol{u}_s^{n+1} - \phi_s^{n+1/2}\boldsymbol{u}_s^{n}}{\Delta t}\right] + \nabla\cdot\left(\phi_s^{n+1}\boldsymbol{u}_s^{n+1}\boldsymbol{u}_s^{n+1}\right) . \tag{13}$$

3. **Prediction & Correction of the velocity field**

   In YALES2, to advance the solution of the Navier-Stokes equations in time, a modified projection method is used based on the Helmholtz-Hodge decomposition presented by Chorin (1968). Keeping the old pressure term in the calculation of the intermediate velocity $\boldsymbol{u}^*$ prevents the introduction of a larger error term making the correction step less computationally demanding (Klainerman and Majda (1982)). The prediction of the intermediate velocity is done as follows:

$$\begin{aligned}\frac{\boldsymbol{u}^* - \boldsymbol{u}^n}{\Delta t} &= -\nabla\cdot(\boldsymbol{u}^*\boldsymbol{u}^n) + \mathscr{P}_s^{n+1} \\ &\quad - \frac{1}{\rho}\nabla P^{n-1/2} + \frac{1}{\rho}\nabla\cdot(\phi_f\boldsymbol{\tau}^n) \\ &\quad + \frac{\chi_s}{\eta}\left(\boldsymbol{u}_s^{n+1} - \boldsymbol{u}^*\right) .\end{aligned} \tag{14}$$

   By subtracting the old pressure gradient from $\boldsymbol{u}^*$, the irrotational part can be written now as:

$$\frac{\boldsymbol{u}^{n+1} - \boldsymbol{u}^*}{\Delta t} = -\frac{1}{\rho}\nabla P^{n+1/2} . \tag{15}$$

   Taking the divergence of the irrotational part and inserting the continuity constraint of Eq. (4), results in the pressure Poisson equation:

$$\nabla^2 P^{n+1/2} = \frac{\rho}{\Delta t}(\nabla\cdot\boldsymbol{u}^* - \mathscr{Q}_s^{n+1}) . \tag{16}$$

   To solve this elliptic equation the deflated preconditioned conjugate gradient (DPCG) solver is used as proposed in Malandain et al. (2013).

Force calculation acting on a solid body in CLIB

Usually with IBM the calculation of the forces acting on the body requires the reconstruction of the solid surface and the integration of the pressure and viscous forces over this surface. The reconstruction of the body surface may prove computationally expensive for complex mobile geometries. In the case of CLIB, the use of the solid volume fraction and the fact that the momentum sources are present inside the solid body and not only at its surface, make the calculation of the total force $\boldsymbol{F}$ trivial. As shown in Lee et al. (2011) the force can be computed by integrating the Navier-Stokes equations over an arbitrary control volume around the solid (which includes the solid):

$$\boldsymbol{F} = \int_{V_s} -\boldsymbol{f}\,\mathrm{d}V + \int_{V_s}\left(\frac{\partial\boldsymbol{u}}{\partial t} + \nabla\cdot(\boldsymbol{u}\boldsymbol{u})\right)\mathrm{d}V , \tag{17}$$

with $\boldsymbol{f}$ representing all the extra momentum sources in Navier-Stokes equations. We can thus avoid reconstructing the solid surface by simply integrating over a volume. By identification, from Eq. (5), we see that $\boldsymbol{f} \equiv \mathscr{P} + \boldsymbol{F}^{\boldsymbol{s}\to\boldsymbol{f}}$. We can thus express the force as the volume integral of the pressure gradient and the divergence of the deviatoric stress inside the solid:

$$\boldsymbol{F} = \int_{\Omega}\phi_s\left(-\frac{1}{\rho}\nabla P + \frac{1}{\rho}\nabla\cdot(\phi_f\boldsymbol{\tau})\right)\mathrm{d}V , \tag{18}$$

where Ω is the computational domain.

3 Validation studies

In this section, several benchmark flow problems are solved using the CLIB method to demonstrate the ability of the method to obtain accurate results for different configurations. We examine three cases of flows around a cylinder of diameter D. The main comparison tools between the numerical results with the reference data are the drag and lift coefficients (C_D and C_L) defined as:

$$C_D = \frac{2F_x}{\rho S U_\infty^2},\quad C_L = \frac{2F_y}{\rho S U_\infty^2} . \tag{19}$$

F_x and F_y are the stream-wise and cross-flow total forces, respectively. U_∞ is the free-stream velocity and S the cross-sectional area of the body.

Flow past a stationary cylinder

The 2D laminar flow past a stationary cylinder is examined first. The aerodynamic coefficients of a two-dimensional cylinder are examined for varying Reynolds numbers ($Re = U_\infty D/\nu$). The inlet velocity is kept constant while the Reynolds number

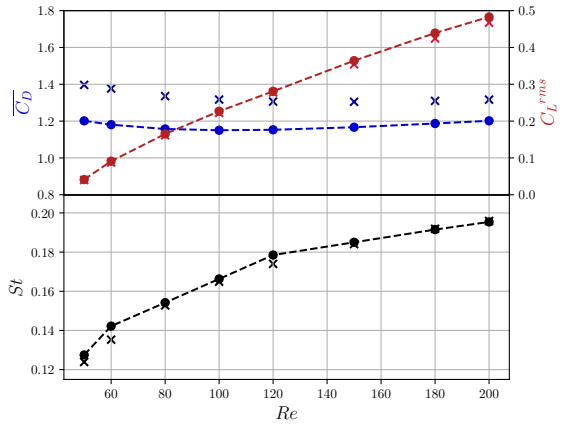

Figure 2: Aerodynamic coefficients and Stouhal number versus Reynolds number: • CLIB, × Qu et al. (2013).

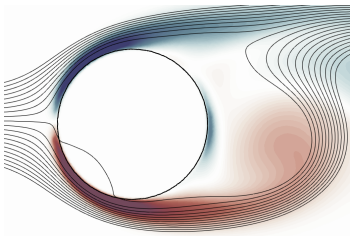

Figure 3: Streamlines for $Re = 200$ and vorticity field $\omega^* = (\nabla \times \boldsymbol{u})D/U_\infty = [-6, 6]$.

2D Sim.	C_L^{rms}	$\overline{C_D}$	ε_D	St
CLIB	1.065	1.513	-	0.234
Jiang and Cheng	1.042	1.521	0.55%	0.239
Henderson	N/A	1.505	0.51%	0.237

Table 1: R.m.s. lift coefficient, time averaged drag coefficient, relative error in mean drag and Strouhal number for $Re = 1000$.

changes according to the values of the varying kinematic viscosity ν. The size of the computational domain is: $\Omega = [-15D, 50D] \times [-15D, 15D]$ containing 1.3 million cells. The solid is placed in a refined region of dimension $[-2D, 10D] \times [-2.5D, 2.5D]$ where the grid spacing is $\Delta_s = 0.01D$. The time-step for all the simulations is determined by a CFL condition set to CFL $= 0.9$. The simulations are carried out for 2000 non-dimensional periods ($t^* = tU_\infty/D$).

Figure 2 shows the lift coefficient mean fluctuation (C_L^{rms}) in excellent agreement with the numerical results of Qu et al. (2013) for all Reynolds number values. It increases rapidly with increasing Re in laminar shedding regimes due to stronger alternate periodic vortex shedding. The Strouhal number $St = f_s D/U_\infty$ (f_s being the vortex shedding frequency) is also in good agreement, although slightly overestimated, following a similar trend with increasing Re.

The mean drag is underestimated for these Reynolds number values. This is directly related to the penalization forcing term since the forcing term $\mathscr{P}_s$ is zero in a stationary solid. Specifically, this underestimation comes from the relatively high values of the penalization time parameter η. Angot et al. (1999) have shown analytically that as $\eta \to 0$ the solution of the penalized equation converges to the solution of the Navier-Stokes equations with the correct boundary conditions at the solid. In our simulations to promote fast solutions and numerical stability, this parameter is equal to the time-step, which gives $\eta = [3.7 \cdot 10^{-5} - 3.2 \cdot 10^{-5}]$ for $Re = [50 - 200]$. As a result the force in the direction of the flow is underevaluated and some fluid streamlines can penetrate inside the solid region (Fig. 3).

The mean drag relative error (ε_D) between CLIB and the reference falls from 14% to 8% as η drops. A two-dimensional simulation for $Re = 1000$ is also carried out and compared to 2D DNS simulations of Jiang and Cheng (2017) and Henderson (1997). In this case, $\eta = 2.5 \cdot 10^{-5}$. All the aerodynamic quantities are in perfect agreement with the reference cases.

Flow past a rotating cylinder

Flow past a rotating cylinder with impulsive start is examined next. The computational domain remains as previously presented. The Reynolds number based on the cylinder diameter and the free-flow velocity is $Re = 200$ and the spin ratio ($\alpha = \omega D/2U_\infty$) ranges between 0 and 5.

The mean lift coefficient is in good agreement with the 2D results of Mittal and Kumar (2003) for lower values of spin ratio. As α increases, the lift magnitude is slightly underestimated. This may be due to the solid velocity into the forcing term $\mathscr{P}_s$ which is weighted by the solid fraction ϕ_s. This leads to an under-predicted fluid velocity at the solid surface ($0 < \phi_s < 1$), hence the effective local spin ratio will be lower. This effect could probably be minimized by increasing the grid resolution near the solid.

The mean drag coefficient is also in good agreement with the reference except for the highest value of spin ratio. As the spin velocity increases, the wake flow deviates from the streamwise direction. For $\alpha =$

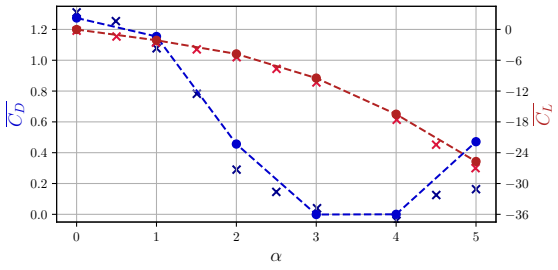

Figure 4: Mean aerodynamic coefficients versus spin ratio: • CLIB, × Mittal and Kumar (2003).

5, the wake is steady but extremely deviated towards the upper and lower boundaries of the domain. In our simulations, these boundaries are located 15 diameters away from the cylinder. Mittal and Kumar (2003) have shown that boundary effects are negligible for distances greater than 75 diameters. Furthermore, the deviation is so extreme that the near wake goes out of the refined-mesh region very quickly, hence influencing the accurate prediction of the wake dynamics.

Cylinder in forced cross-flow oscillation

Numerical simulations of flow past a cylinder forced to oscillate in the cross-flow direction is presented here for a fixed Reynolds number of 500. The computational domain remains unchanged. A sinusoidal motion is prescribed to the solid with an amplitude of oscillation normalized by the cylinder diameter $A = y_{\max}/D$ and an excitation frequency $f_0 = 1/T_0$. The non-dimensional solid motion is described by:

$$\gamma(t) = A\sin(2\pi f_0 t)\,. \tag{20}$$

The fluid flow can be affected by the cylinder motion producing different regimes depending on the frequency ratio $F = f_0/f_s$. In our case the values of F are based on the shedding frequency $f_s = 22.15$ Hz found in a simulation with a stationary cylinder at $Re = 500$. The simulation was carried out for 2000 non-dimensional periods.

The reference case used is a 2D LES simulation of Blackburn and Henderson (1999) where the following configurations are examined: $(A; F) = (0.25; [0.75 - 1.05])$. This range of frequency ratios is particularly interesting since many complex physical phenomena take place around $F = 1$. One such phenomenon is the lock-in regime where the vortex shedding frequency and cross-flow oscillation frequency coalesce. In the forced oscillation case, the vortex shedding frequency changes to match the cylinder's oscillation. Inside the lock-in regime, depending on F, there is a notable change in the timing of the vortex shedding with respect to the cylinder motion. This effect is related to a sign change in the non-dimensional mechanical energy transferred between the fluid and the solid per motion cycle which can be expressed as:

$$E = \int_0^{T_0} C_L \cdot \dot{\gamma}\,\mathrm{d}t\,. \tag{21}$$

This quantity takes negative values when energy is transferred from the solid to the fluid and positive when energy is transferred to the solid. As discussed in Blackburn and Henderson (1999) previous experimental studies show that the sign switch happens between two limit values of F that depend on both the Reynolds number and the amplitude of oscillation. For their simulation at $Re = 500$ and $A = 0.25$ the switch takes place at around $F = 0.85$ and ends at $F = 0.95$. The evolution of the energy E with F predicted using the CLIB method is shown in Fig. 5. We see a slight

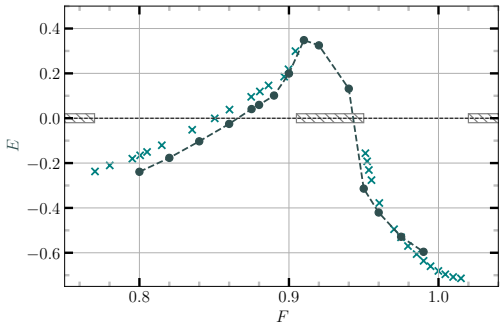

Figure 5: Energy transfer between solid and fluid versus frequency ratios: • CLIB, × Blackburn and Henderson (1999).

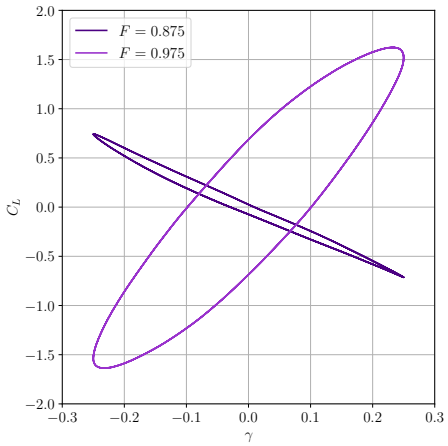

Figure 6: Limit cycles of C_L versus γ below the phase switch ($F = 0.875$) and above ($F = 0.975$).

underestimation of the energy at lower oscillation frequencies. This can be attributed once again to penetrating fluid streamlines in the direction of motion, and thus the underestimation of the lift coefficient.

The switch in energy sign is accompanied by a change in the phase difference $\phi_{L-\gamma}$ between lift and displacement. Starting from a phase difference of 180°, it approaches rapidly to 90° near $F = 0.9$. Then at $F = 0.95$ the phase difference jumps to 0° where the lift follows perfectly the displacement. We successfully observe the phase switch from the lift cycles computed with the CLIB method. Figure 6 shows two cases where $\phi_{L-\gamma} \approx 180°$ and 0° for $F = 0.875$ and 0.975, respectively. In the region of $F = [0.91 - 0.95]$ the flow presents a weakly chaotic regime where some rapid changes in energy sign are observed. The average value however per cycle showed the biggest energy transfer from the fluid to the solid.

Lagrangian solid and mass conservation

For the previous simulations fine meshes were used, but for higher Reynolds number values compromises on the grid resolution will have to be made. To demonstrate that the Lagrangian particles conserve the solid mass independently of the fluid mesh resolution

and the movement of the solid, we solved the flow past a 2D cylinder of diameter D and volume V_{cyl}, oscillating with amplitude $y_{\max} = D$. Since the density of the solid is constant, the relative error between the computed volume $\left(V_s(t) = \int_\Omega \phi_s(t)\,\mathrm{d}V\right)$ and theoretical volume V_{cyl} is examined for two coarse grids where $\Delta_s = D/5$ and $D/10$. The mean relative error is $0.16 \pm 2.11 \cdot 10^{-14}$ % and $0.16 \pm 1.38 \cdot 10^{-14}$ %, respectively. Hence, the influence of the grid resolution is essentially negligible on the solid mass conservation. The conservative nature of the solid volume fraction in turn guaranties the conservation of the fluid mass as well inside a given computational domain. Future studies will focus on the limits of CLIB to predict accurate aerodynamic parameters on coarser grids.

4 Conclusions

A conservative Lagrangian immersed boundary method coupling a VOS approach with the penalty method has been proposed for solving incompressible viscous flow problems around stationary or mobile solid geometries. Three 2D validation cases have been performed: flow past a stationary, a rotating and an oscillating cylinder. The Lagrangian representation of the solid volume fraction field makes the conservation of the solid and fluid mass independent of the grid resolution. Concerning the prediction of the aerodynamic quantities, a good agreement with literature has been observed despite a slight underestimation in some cases. Two main factors have been identified. The force at the body surface may be underestimated because the solid velocity is weighted by the non-unity solid fraction at solid interface in the momentum equation. Another aspect is the parameter η of the penalty term which is essentially the value of the time-step Δt. All the simulations were driven by a high CFL value constraint which gave large time-steps in the validation cases. With smaller time-steps, the penalty forcing term will decrease, solving the penetrating streamlines issue. Future work will seek to improve the estimation of the forces. It will also include the implementation of the method in three-dimensional flows for wind energy applications. Furthermore, the computational performances of the method will be tested and compared against the costly and computationally demanding body-fitted arbitrary Lagrangian-Eulerian (ALE) method coupled with dynamic mesh adaptation for complex solid geometries in motion.

Acknowledgments

This work was granted access to HPC resources from IDRIS, France under the allocation A0082A11335 via GENCI.

References

Angot, P., Bruneau, C. H. and Fabrie, P. (1999) A penalization method to take into account obstacles in incompressible viscous flows, *Numerische Mathematik*, 81(4), pp. 497–520.

Blackburn, H. M. and Henderson, R. D. (1999) A study of two-dimensional flow past an oscillating cylinder, *Journal of Fluid Mechanics*, 385, pp. 255–286.

Chorin, A. J. (1968) Numerical solution of the Navier-Stokes equations, *Mathematics of Computation*, 22(104), pp. 745–745.

Henderson, R. D. (1997) Nonlinear dynamics and pattern formation in turbulent wake transition, *Journal of Fluid Mechanics*, 352, pp. 65–112.

Hirt, C. W. and Nichols, B. D. (1981) Volume of fluid (VOF) method for the dynamics of free boundaries, *Journal of Computational Physics*, 39(1), pp. 201–225.

Jiang, H. and Cheng, L. (2017) Strouhal-Reynolds number relationship for flow past a circular cylinder, *Journal of Fluid Mechanics*, 832, pp. 170–188.

Klainerman, S. and Majda, A. (1982) Compressible and incompressible fluids, *Communications on Pure and Applied Mathematics*, 35(5), pp. 629–651.

Kraushaar, M. (2012) Low-mach number approaches to large-eddy simulation of turbulent flows in aero-engines, Fluids mechanics [physics.class-ph]. Institut National Polytechnique de Toulouse - INPT.

Lee, J. et al. (2011) Sources of spurious force oscillations from an immersed boundary method for moving-body problems, *Journal of Computational Physics*. Academic Press Inc., 230(7), pp. 2677–2695.

Liu, R. K. S., Ng, K. C. and Sheu, T. W. H. (2021) A volume of solid implicit forcing immersed boundary method for solving incompressible Navier-Stokes equations in complex domain, *Computers and Fluids*. Elsevier Ltd, 218.

Malandain, M., Maheu, N. and Moureau, V. (2013) Optimization of the deflated Conjugate Gradient algorithm for the solving of elliptic equations on massively parallel machines, *Journal of Computational Physics*, 238, pp. 32–47.

Mittal, S. and Kumar, B. (2003) Flow past a rotating cylinder, *Journal of Fluid Mechanics*, 476(476), pp. 303–334.

Moureau, V., Domingo, P. and Vervisch, L. (2011) Design of a massively parallel CFD code for complex geometries, in *Comptes Rendus - Mecanique*, pp. 141–148.

Muldoon, F. and Acharya, S. (2005) Mass conservation in the immersed boundary method, *Proceedings of 2005 ASME Fluids Engineering Division Summer Meeting, FEDSM2005, 2005*, pp. 821–829.

Peskin, C. S. (1972) Flow patterns around heart valves: A numerical method, *Journal of Computational Physics*, 10(2), pp. 252–271.

Porté-Agel, F., Bastankhah, M. and Shamsoddin, S. (2019) Wind-Turbine and Wind-Farm Flows: A Review, Boundary-Layer Meteorology. *Springer Netherlands*.

Qu, L. et al. (2013) Quantitative numerical analysis of flow past a circular cylinder at Reynolds number between 50 and 200, *Journal of Fluids and Structures*, 39(28), pp. 347–370.

Sotiropoulos, F. and Yang, X. (2014) 'Immersed boundary methods for simulating fluid-structure interaction', *Progress in Aerospace Sciences*, 65, pp. 1–21.

Uhlmann, M. (2005) An immersed boundary method with direct forcing for the simulation of particulate flows, *Journal of Computational Physics*, 209(2), pp. 448–476.

Zhang, C. et al. (2014) A sharp interface immersed boundary/VOF model coupled with wave generating and absorbing options for wave-structure interaction, *Computers and Fluids*, 89, pp. 214–231.